

# Plasma sheet access to geosynchronous orbit

H. Korth, M. F. Thomsen, J. E. Borovsky, and D. J. McComas

Los Alamos National Laboratory, Los Alamos, New Mexico

**Abstract.** One year’s worth of magnetospheric plasma analyzer data from three Los Alamos geosynchronous satellites are used for a statistical study of proton and electron fluxes at geosynchronous orbit and their dependence on local time (LT) and geomagnetic activity level as measured by  $Kp$ . When displayed as a function of LT and  $Kp$ , the fluxes exhibit distinct boundaries, which are shown to be consistent with a combination of a global pattern of particle drift through the magnetosphere and loss processes mainly due to charge exchange of the ions and auroral precipitation of the electrons. A Hamiltonian energy conservation approach combined with the  $(U, B, K)$  coordinate transformation introduced by *Whipple* [1978] is used to calculate the theoretical position of the separatrix between open and closed drift trajectories (Alfvén layer) as a function of particle species, energy, local time, and geomagnetic activity level. The comparison of the theoretical boundaries with the observations confirms the predictions of plasma sheet access to the geosynchronous region. The analysis also provides independent statistical support for previously derived relationships between  $Kp$  and the strength of the global convection electric field.

## 1. Introduction

The plasma sheet represents an important region in the Earth’s magnetosphere that is the source of the higher-energy particle population that is injected into the inner magnetosphere during magnetic substorms [e.g., *DeForest and McIlwain*, 1971; *McComas et al.*, 1993; *Birn et al.*, 1997; *Kerns et al.*, 1994; *Burke et al.*, 1995; *Liemohn et al.*, 1998]. Furthermore, the plasma sheet is believed to be the direct source of ring current particles [e.g., *Smith et al.*, 1979; *Chen et al.*, 1994]. For this reason many ring current simulations have used the plasma sheet properties as an outer boundary condition for their calculations [e.g., *Wolf et al.*, 1982; *Chen et al.*, 1994; *Fok et al.*, 1996]. The simulations have shown that the plasma sheet density has a direct influence on the strength of the ring current. More recent simulations actually use geosynchronous observations as boundary conditions [*Jordanova et al.*, 1998; *Kozyra et al.*, 1998b]. Such measurements provide a direct means of determining whether or not in any given event the plasma sheet has access to geosynchronous orbit and hence to the inner magnetosphere. The purpose of this study is to explore on a statistical basis the conditions under which plasma sheet material has access to geosynchronous orbit and to compare that statistical assessment with the expectations based on a simple model of con-

vective transport in the inner magnetosphere.

In this study we expand on previous work by *Maurice et al.* [1998], who examined the hot-ion properties at geosynchronous orbit under quiet magnetospheric conditions. We use a large database of magnetospheric plasma analyzer (MPA) data collected from Los Alamos geosynchronous satellites to address statistically the question of the access of plasma sheet material to geosynchronous orbit and its dependence on local time and geomagnetic activity. The observations are compared with the access predicted for particle drifts in global magnetic and electric fields. We find that the plasma sheet particles do, in fact, have access to geosynchronous orbit, except for particles with higher energies during times of very low magnetic activity. Moreover, on a statistical basis, the access of particles to this region can be understood with the conventional drift paradigm, and the  $Kp$  index provides an appropriate proxy for the strength of the convection.

## 2. Particle Drift Description

The guiding-center drift velocity of a particle within the Earth’s magnetosphere can be expressed as [*Kivelson and*

Russell, 1995, p. 307]

$$\mathbf{v}_D = \frac{\mathbf{E} \times \mathbf{B}}{B^2} + \frac{\mathbf{F}_{\text{ext}} \times \mathbf{B}}{qB^2} + \frac{W_{\text{kin},\perp} \mathbf{B} \times \nabla B}{qB^3} + \frac{2W_{\text{kin},\parallel} \hat{\mathbf{r}}_c \times \mathbf{B}}{qR_c B^2}, \quad (1)$$

where  $\mathbf{E}$  is the macroscopic electric field;  $\mathbf{B}$  is the magnetic field;  $\mathbf{F}_{\text{ext}}$  represents an external force;  $W_{\text{kin},\parallel} = \frac{1}{2}mv_{\parallel}^2$  and  $W_{\text{kin},\perp} = \frac{1}{2}mv_{\perp}^2$  are the particle's kinetic energies parallel and perpendicular to  $\mathbf{B}$ , respectively;  $R_c$  is the radius of curvature of the magnetic field line; and  $\hat{\mathbf{r}}_c$  is a unit vector outward from the center of curvature. The terms in (1) are called  $\mathbf{E} \times \mathbf{B}$  drift, external-force drift, gradient drift, and curvature drift.

The complex drift trajectories resulting from (1) can be well described by a Hamiltonian energy conservation approach with an appropriate coordinate transformation [Whipple, 1978]. The main idea is the following: If a particle of arbitrary charge, energy, and pitch angle conserves the first two adiabatic invariants, it also conserves its total energy [e.g., Kivelson and Russell, 1995, pp. 308–309]. For a time-stationary magnetic field (hence neglecting any inductive electric fields) the electric field can be written as the gradient of a scalar potential  $U$ . Thus the total energy is

$$W_{\text{tot}} = qU + W_{\text{kin}} = qU + \mu B_m, \quad (2)$$

where  $B_m(K)$  is the magnetic field intensity at the mirror point,  $K$  is the modified second invariant [e.g., Taylor and Hones, 1965; Roederer, 1970], and  $\mu = 1/2 mv_{\perp}^2/B$  is the magnetic moment. Owing to the conservation of total energy, a coordinate transformation into the  $(U, B, K)$  space leads to simple drift trajectories [Whipple, 1978], since  $dW/dt = 0 = d(\mu B_m)/dt + d(qU)/dt$  results in

$$\frac{\partial U}{\partial B_m} = -\frac{\mu}{q}. \quad (3)$$

Equation (3) states that all particle drift trajectories in the  $(U, B, K)$  space are straight lines with the slope  $-\mu/q$ . For a dipole magnetic field and a shielded cross-tail plus corotation electric field, the mapping into the  $(U, B, K)$  space is double valued [cf. Whipple, 1978]. This ambiguity can be resolved by splitting the magnetosphere into a dayside and a nightside. The boundary between the two halves of the magnetosphere is the locus of all points where the magnetic field intensity reaches an extremum on the equipotentials. For the electric field models considered in this study, the separator is the dawn-dusk meridian.

The potential configuration due to superposition of a shielded cross-tail field with a corotation field is

$$U(r, \phi) = -\frac{a}{r} - br^{\gamma} \sin(\phi), \quad (4)$$

where  $r$  is the distance from the center of the Earth,  $\phi$  is the magnetic local time referred to noon rather than midnight,  $\gamma$  is the shielding exponent, and  $a = 92.4 \text{ kV } R_E$  is the corotation constant [e.g., Southwood and Kaye, 1979]. The shielding exponent was proposed by Volland [1973] and Stern [1975] and has been estimated by these authors to be  $\sim 2$ . This result was confirmed by various authors [e.g., Maynard and Chen, 1975; Ejiri, 1978; Ejiri et al., 1978; Southwood and Kaye, 1979; Elphic et al., 1999]. The coefficient  $b$  determines the cross-tail electric field strength, which varies with the level of geomagnetic activity. A number of authors have expressed  $b$  as a function of the  $Kp$  index. The present study provides an independent assessment of the suitability of some of these parametrizations.

As pointed out by many authors, a potential function of the form of (4) produces two classes of equipotentials: Near the Earth there is a class of potential contours which are continuous around the Earth, corresponding to cold-plasma drift trajectories that are closed; at larger distances, the potential contours extend from the geomagnetic tail, in toward and around the closed-contour region and out to the dayside magnetopause. At dusk the separatrix between open and closed equipotentials corresponds to a stagnation point in the flow, i.e.,  $\partial U/\partial r = 0$ . Using (4), the distance at 1800 LT to this separatrix between open and closed cold-plasma drift trajectories is found to be

$$r_s = \left( \frac{a}{\gamma b} \right)^{\frac{1}{\gamma+1}}. \quad (5)$$

At midnight the radial distance to the separatrix equipotential is related to  $r_s$  through (4):

$$r_m = \frac{r_s}{1 + \frac{1}{\gamma}}. \quad (6)$$

Combining (5) and (6) provides a relationship between the cross-tail electric field intensity and the equatorial distance of the separatrix at midnight:

$$b = \frac{a}{\gamma \left(1 + \frac{1}{\gamma}\right)^{\gamma+1} r_m^{\gamma+1}}. \quad (7)$$

The nightside separatrix should approximately mark the inner edge of the electron plasma sheet [e.g., Elphic et al., 1999, and references therein]. As argued by previous authors, the inner edge of the electron plasma sheet maps down to the equatorward boundary of the auroral oval [Gussenhoven et al., 1981, 1983]. Denoting the invariant latitude of this boundary at midnight as  $\lambda_m$ , we thus obtain for a dipole field:

$$b = \frac{a}{\gamma \left(1 + \frac{1}{\gamma}\right)^{\gamma+1}} (\cos^2 \lambda_m)^{\gamma+1}. \quad (8)$$

The latitude of the equatorward edge of the diffuse aurora has been determined from DMSP measurements of precipitating plasma sheet electrons and has been shown to be well correlated with  $Kp$  [Gussenhoven *et al.*, 1981, 1983]. From a large body of DMSP measurements, Gussenhoven *et al.* found the empirical relationship  $\lambda_m = 67.8 - 2.07 Kp$ . Inserting this expression into (8) thus provides a method for obtaining the cross-tail electric field, which will be referred to as the Gussenhoven method.

Another parametrization for the cross-tail electric field was derived by Maynard and Chen [1975] from Ogo 3 and 5 midnight plasmopause crossing data. For a shielding exponent  $\gamma = 2$  the cross-tail electric field dependence on the  $Kp$  index was found to be  $b = 0.045/(1 - 0.159 Kp + 0.0093 Kp^2)^3$ . This expression for the strength of the convection field will be referred to as the Maynard method in this paper.

For simplicity we now consider only equatorially mirroring particles. As a result the modified second adiabatic invariant  $K$  is zero at all times and hence can be ignored. We note that a comparison of this simplification with the observations will not be strictly valid since our study involves spin-averaged flux data. However, the observed ratio of perpendicular to parallel temperature is usually greater than 1 ( $T_\perp/T_\parallel = 1.25$  (median), 1.12 (25th percentile), 1.36 (75th percentile)), indicating that pitch angles closer to  $90^\circ$  are favored, so the  $K = 0$  assumption should still provide a reasonable comparison.

With a dipole magnetic field in the equatorial plane given by  $B(r, \phi) = B_E/r^3$ , the potential at the dawn-dusk terminator becomes

$$U(B) = \pm b \left( \frac{B_E}{B} \right)^{\frac{2}{3}} - a \left( \frac{B}{B_E} \right)^{\frac{1}{3}}, \quad (9)$$

where the positive sign represents the dawn terminator and the negative sign gives the dusk terminator.

Within this drift scenario, particle fluxes should be organized by the boundaries between open and closed drift trajectories. These boundaries are known as Alfvén layers [e.g., Schield *et al.*, 1969, and references therein] and can be identified in the  $(U, B)$  space as the straight lines (3) that are tangent to the curves (9) [Whipple, 1978]. By transforming the coordinates of these straight lines from the  $(U, B)$  space back into the Cartesian space, the Alfvén layers for protons and electrons are obtained. Figures 1 and 2 (left and middle) show the Alfvén boundaries derived for various energies at  $Kp = 0$  and  $Kp = 4$  evaluated with the Gussenhoven  $\gamma = 2$  model. The Earth is shown in the center of each graph, and the dashed circle is the location of geosynchronous orbit at a distance of  $6.6 R_E$  from the Earth's center. Figures 1 and 2 (right) show the corresponding local time of

the Alfvén boundary at geosynchronous orbit for  $Kp$  ranging from 0 to 9. The shaded regions show the local time ranges for which geosynchronous orbit lies inside the separatrices, on closed drift paths. For example, Figures 1 and 2 show that at low values of  $Kp$  (i.e., for weak convection), the higher-energy position of the plasma sheet population does not have access to geosynchronous orbit.

### 3. Instrumentation and Data Analysis

Since 1989, Los Alamos National Laboratory has fielded magnetospheric plasma analyzers on several satellites in geosynchronous orbit. The MPA instrument is an electrostatic analyzer measuring three-dimensional energy per charge distributions of ions and electrons. The energy range extends from  $\sim 1$  eV/ $q$  to  $\sim 40$  keV/ $q$ . A detailed instrument description is given by Bame *et al.* [1993] and McComas *et al.* [1993]. The routine processing of MPA data includes the calculation of several moments of the particle distributions, as well as spin-averaged fluxes at each of the 40 energy levels for both electrons and ions. These products are archived separately from the full three-dimensional distributions. This reduced data set forms the basis of the present work. For this study we use 1 year's worth of data (1996) from three different satellites, corresponding to approximately 1 million data points with a time spacing of 86 s on each satellite.

The data are processed in the following way: The data points for each half hour of local time covered by one satellite on a given day are extracted from the database, and the median of the observed parameter is calculated. By calculating the median instead of the average value, outliers in the measurements are eliminated. (Calculations using the average value do not lead to significant differences in the statistics.) Magnetosheath and boundary layer intervals are excluded by accepting only measurements with a proton density of  $< 3 \text{ cm}^{-3}$  and a perpendicular proton temperature of  $> 2000$  eV. The half-hour median values are then sorted into bins according to local time and geomagnetic activity, represented by the  $Kp$  index. Finally, for each LT- $Kp$  bin, the average of all the median values is calculated.

The distribution of data points included in each  $Kp$  bin is equal to the  $Kp$  occurrence distribution shown in Figure 3. The distribution in LT for each  $Kp$  range was fairly uniform, so Figure 3 provides a good indication of the significance of the derived values in various  $Kp$  ranges. In general, the best statistical representation is achieved for the most common geomagnetic activity levels in the  $Kp$  range from 1– to 3. The better statistics in this activity range will be manifested as smoother transitions between the bins in the distributions presented below. Figure 3 also indicates that 1996 was a

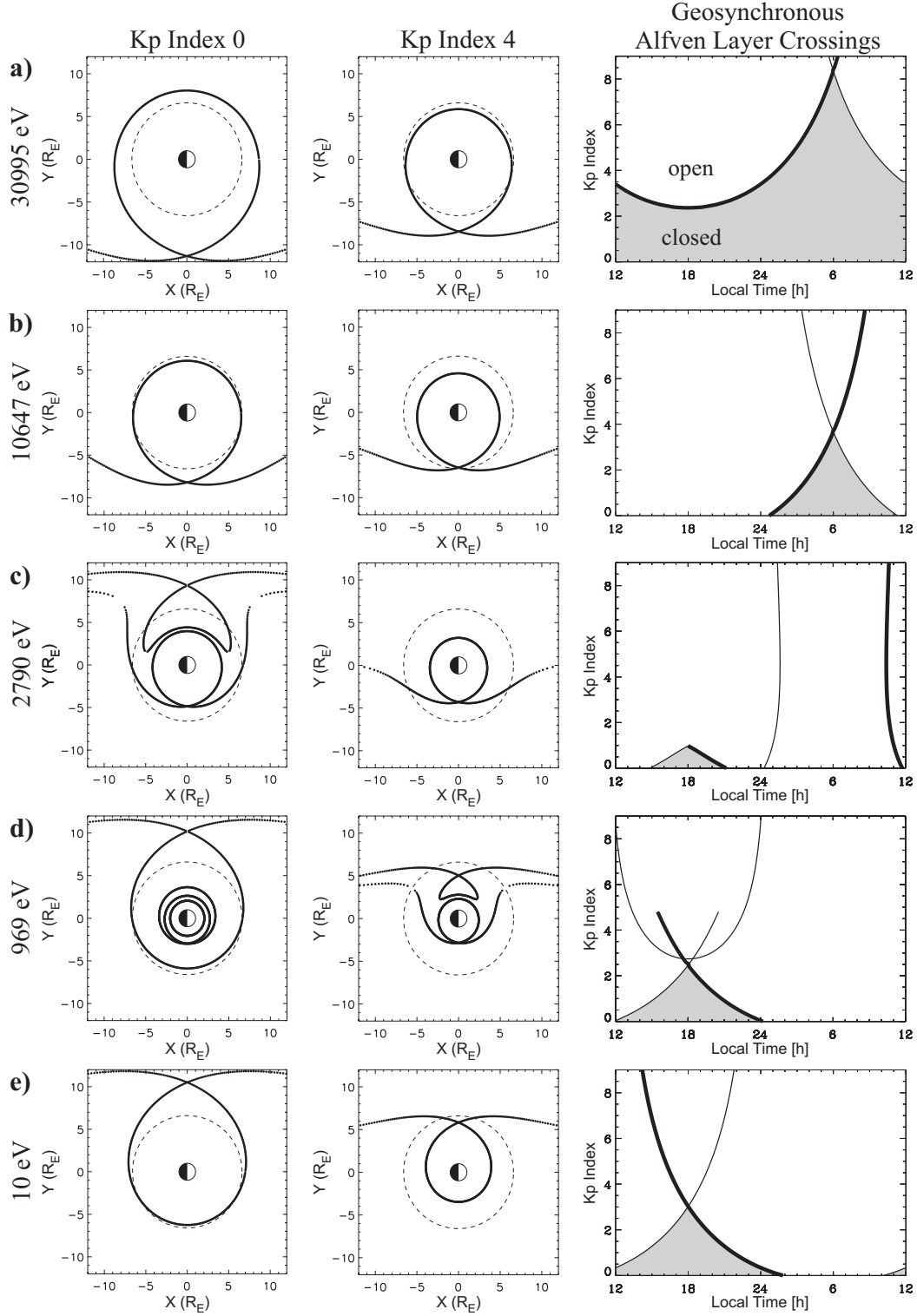


**Figure 1.** Open/closed drift separatrices for different energy protons, (a) 30,995 eV, (b) 10,647 eV, (c) 2790 eV, (d) 969 eV, and (e) 10 eV, calculated assuming a cross-tail electric field that is parameterized by  $Kp$ , for  $Kp =$  (left) 0 and (middle) 4. (right) LT and  $Kp$  dependence of the geosynchronous crossings of the separatrices. The  $Kp$  dependence of the convection field strength is based on the Gussenhoven model for  $\gamma=2$ . Areas of closed drift paths are shaded at right.

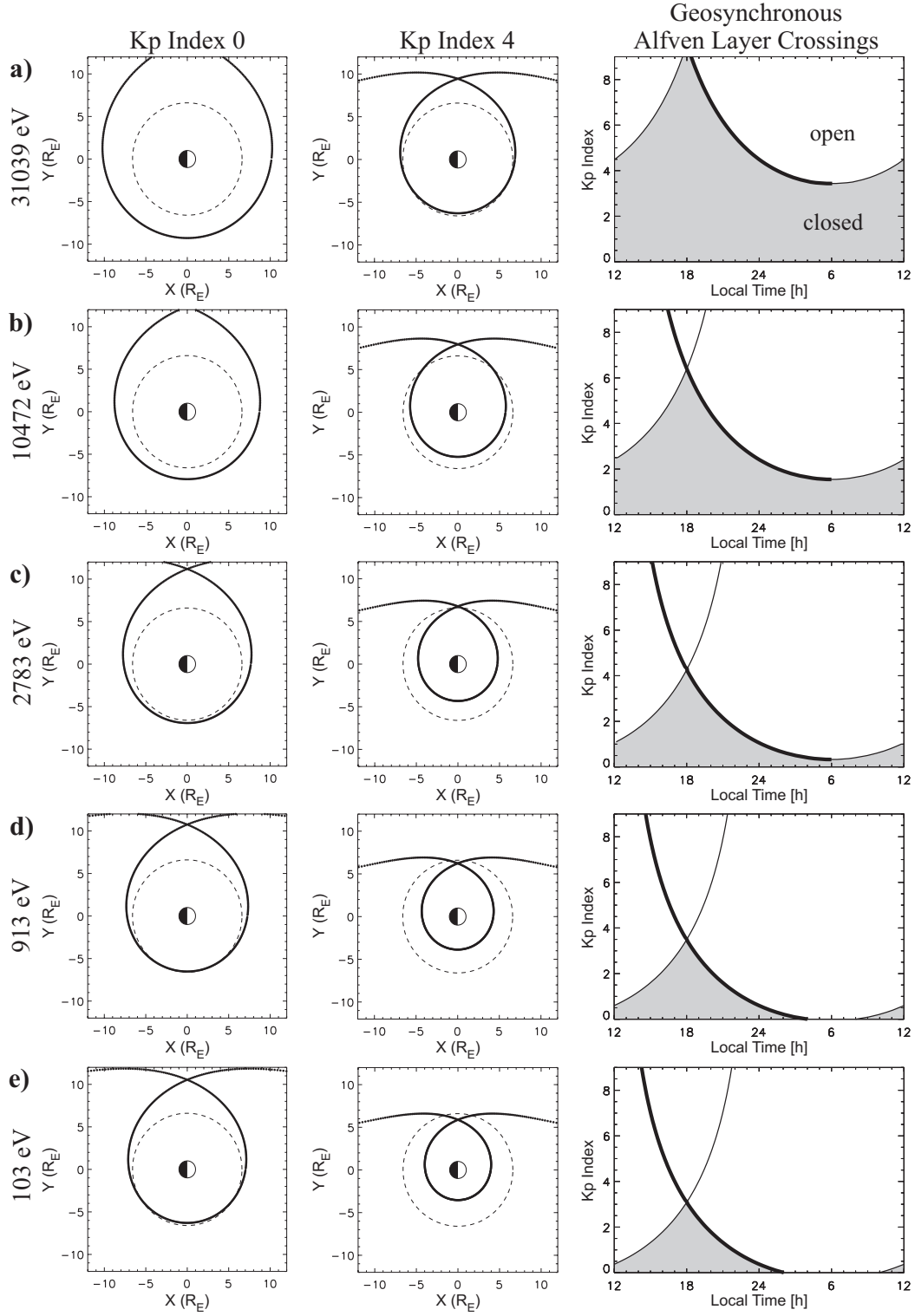


**Figure 2.** Open/closed drift separatrices for different energy electrons, (a) 31,039 eV, (b) 10,472 eV, (c) 2783 eV, (d) 913 eV, and (e) 103 eV, calculated assuming a cross-tail electric field that is parameterized by  $Kp$ , for  $Kp$  = (left) 0 and (middle) 4. (right) LT and  $Kp$  dependence of the geosynchronous crossings of the separatrices. The  $Kp$  dependence of the convection field strength is based on the Gussenhoven model for  $\gamma=2$ . Areas of closed drift paths are shaded at right.

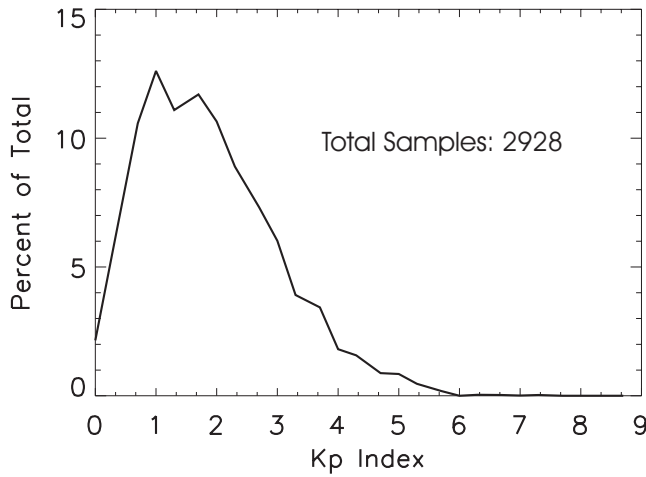


**Figure 3.** Occurrence frequency of  $Kp$  for 1996.

relatively low  $Kp$  year.

#### 4. Observations

The results from the statistical analysis of spin-averaged proton and electron fluxes are displayed in a special form which can be understood with the help of an example shown in Plate 1 for the proton flux of the 30,995 eV channel. As mentioned in section 2 the geosynchronous Alfvén layer crossings at various geomagnetic activity levels (Plate 1a, adapted from Figure 2a, left and middle) can be transformed into a representation of the crossings as a function of local time and  $Kp$  (Plate 1b, adapted from Figure 2a, right). For easier differentiation between the open and closed drift trajectory regions, the closed regions are shaded. The curves in Plates 1a and 1b represent the Gussenhoven  $\gamma = 2$  model.

In Plate 1c the LT/ $Kp$  locus of the Alfvén layer crossings from Plate 1b, as well as for the other convection models we have examined, is overlaid onto the LT/ $Kp$  distribution of average fluxes, compiled as described above. The fluxes are color coded according to the color bar shown next to the graph. The black regions indicate data unavailability, and white bins contain flux values exceeding the maximum of the corresponding color bar.

The average observed fluxes for various energies of protons and electrons are shown in Plates 2 and 3, respectively, in the same manner as illustrated in Plate 1c. The corresponding drift separatrices for each energy level, as well as the LT/ $Kp$  dependence of the geosynchronous Alfvén layer crossings, can be found in Figure 1 for the protons and Figure 2 for the electrons.

Distinct boundaries are evident in the fluxes displayed in Plates 2 and 3. Some of these boundaries appear to coin-

cide with the calculated open-closed drift boundaries. The sections of the calculated curves that appear to correspond to apparent boundaries in the observed fluxes are marked as thick lines in Figures 1 and 2. We now consider in more detail the implications of these comparisons.

##### 4.1. Protons

In Plate 2a the proton fluxes for the high-energy channel (30,995 eV) are low at all local times for low  $Kp$  values. As shown in Figure 1, under low-activity conditions, geosynchronous orbit should lie entirely within the region of closed drift trajectories for particles of this energy and should thus be inaccessible to fresh plasma sheet material, consistent with the observed low fluxes. With rising geomagnetic activity the Alfvén layer moves closer and closer to the Earth, giving the plasma sheet access to geosynchronous orbit at an increasing range of local time centered at dusk. Consistent with this expectation, higher fluxes in this energy range are indeed observed at these local times, and the flux boundary is generally well described by the calculated boundary between open and closed drift paths at most local times. The exception is a region before noon where the fluxes are substantially lower than in the open drift path region on the nightside. More will be said below about this apparent depletion, which was also noted by McIlwain [1972]. The models best representing the statistical flux distribution are the curves using the Gussenhoven  $\gamma = 3$  method and the Maynard method.

For the next lower proton energy, 10,647 eV (Plate 2b), the models predict that open drift trajectories have access to geosynchronous orbit in the premidnight region at low  $Kp$  values. The observed flux boundary is in remarkably good correspondence with this expectation, showing a clear drop in the flux rate around midnight at the predicted transition from open to closed drift trajectories. Above a  $Kp$  of  $\sim 3$  the model predicts that geosynchronous orbit should lie on open drift trajectories at all local times. Thus we would expect to see plasma sheet flux levels at all local times. Instead, the flux rates at high  $Kp$  show the same drop at increasing local times as the ones at lower geomagnetic activity levels. This behavior can be interpreted, through reference to Figure 1, as evidence for the action of significant loss processes during the drift through the near-Earth region (see also Maurice *et al.* [1998] and Kistler *et al.* [1989]). The obvious flux boundary in Plate 2b clearly corresponds to the thick curve shown in Figure 1b (right). By comparison with Figure 1b (middle), it can be seen that this boundary separates drift trajectories that take a direct dawnside route from trajectories that follow the long, circuitous route around the duskside of the Earth. Plasma sheet ions taking the long route have a longer time to suffer losses and hence reach the prenoon

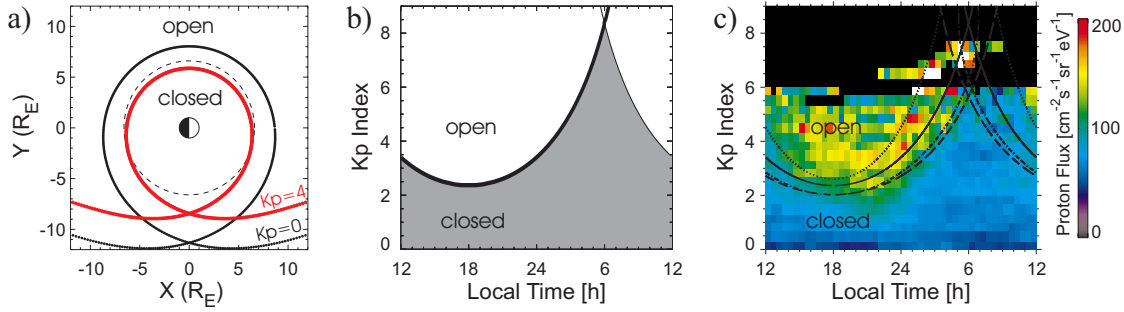


**Plate 1.** Illustration of drift-trajectory analysis of geosynchronous flux occurrence statistics for protons with an energy of 30,995 eV. (a) Open/closed drift separatrices in the equatorial plane for 30,995 eV protons for  $Kp = 0$  and  $Kp = 4$ . (b) Corresponding LT/ $Kp$  locus of the Alfvén layer crossings calculated by the Gussenhoven  $\gamma = 2$  model. (c) Curves of the geosynchronous Alfvén layer crossings for different models, overlaid on the average fluxes measured in this energy channel. The dotted, solid, and dashed curves represent shielding factors  $\gamma = 1, 2, 3$ , respectively, for the Gussenhoven model; the Maynard  $\gamma = 2$  model is shown as a dash-dotted curve.

sector with significantly lower fluxes. These loss processes themselves cannot be explained by the Alfvén layer model, but the transition between the open drift trajectory region of fresh proton plasma passing the Earth at dawn and the open drift trajectories of depleted protons moving clockwise around the Earth produces a clearly observed flux boundary. The depletion suffered by the protons is principally caused by atmospheric losses, charge exchange, and Coulomb collisions [e.g., Kistler *et al.*, 1989; Fok *et al.*, 1991; Jordanova *et al.*, 1996; Kozyra *et al.*, 1998a]. In the energy range of our study, charge exchange is the most important loss process for protons [Fok *et al.*, 1991; Jordanova *et al.*, 1996]. The observed boundary in Plate 2b appears to be best modeled using the Gussenhoven  $\gamma = 2, 3$  and the Maynard methods.

At an ion energy of 2790 eV the theoretical separatrices illustrated in Figure 1c become complicated, especially at lower  $Kp$ . Close inspection shows that there is, nonetheless, a good correspondence between the predicted boundaries and the flux observations shown in Plate 2c. In Plate 2c the region of closed “banana” orbits predicted near dusk at low  $Kp$  is clearly absent of significant fluxes. The clear boundary just before noon corresponds to the transition from paths that bring fresh plasma sheet material rather directly around the dawn side to the longer drift paths taken by plasma sheet ions coming around the dusk side (see Figure 1). As discussed above, the flux drop at this boundary is again indicative of appreciable losses during the drift from the nightside. The predicted “boundary” near midnight does not correspond to any flux discontinuity (Plate 2c) because it is a boundary based on the future motion of the particles (whether they will go to dawn or dusk), rather than a boundary in the source properties. None of the convection models appears particularly superior for this energy range.

For protons of lower energies ( $\lesssim 1$  keV) the bulge of the closed orbit region is found at dusk instead of dawn (Figure 1d), consistent with the observed low proton fluxes at 969 eV in the evening sector at  $Kp < 3$  (Plate 2d). At higher  $Kp$ , when the Alfvén layer is completely earthward of geosynchronous orbit and banana orbits exist, a dark lane occupies the region between the two afternoon separatrices. From Figure 1d, it is apparent that this region corresponds to drift paths that are very circuitous and probably exposed to significant losses for a long time. At this energy the Gussenhoven  $\gamma = 2$  method leads to the closest fit to the statistical boundary.

Temporarily postponing our discussion of Plate 2e, we first turn to Plate 2f, which shows the statistical distribution of proton fluxes between 1 and 10 eV. This flux distribution in this energy range is essentially a mirror image of the 30 keV channel: The closed drift trajectories have the high fluxes, while the open drift trajectories are essentially empty, at least on the nightside. This mirror image reflects the different sources of the low- and high-energy ion populations: The high-energy protons originate in the plasma sheet, whereas the cold particles originate in the ionosphere and are only able to achieve significant flux levels in the region where flux tubes can circulate many times around the Earth, i.e., the plasmasphere [e.g., Nishida, 1966]. The presence of significant cold-proton fluxes on presumably open drift trajectories in the afternoon sector is attributable to plasmaspheric drainage and plasmasphere refilling processes. Drainage occurs when a rapidly increasing convection electric field moves the zero-energy Alfvén layer closer to the Earth, so that dense, cold plasma that was previously on closed drift trajectories finds itself on open drift trajectories that drain to the magnetopause [e.g., Chen and Gre-

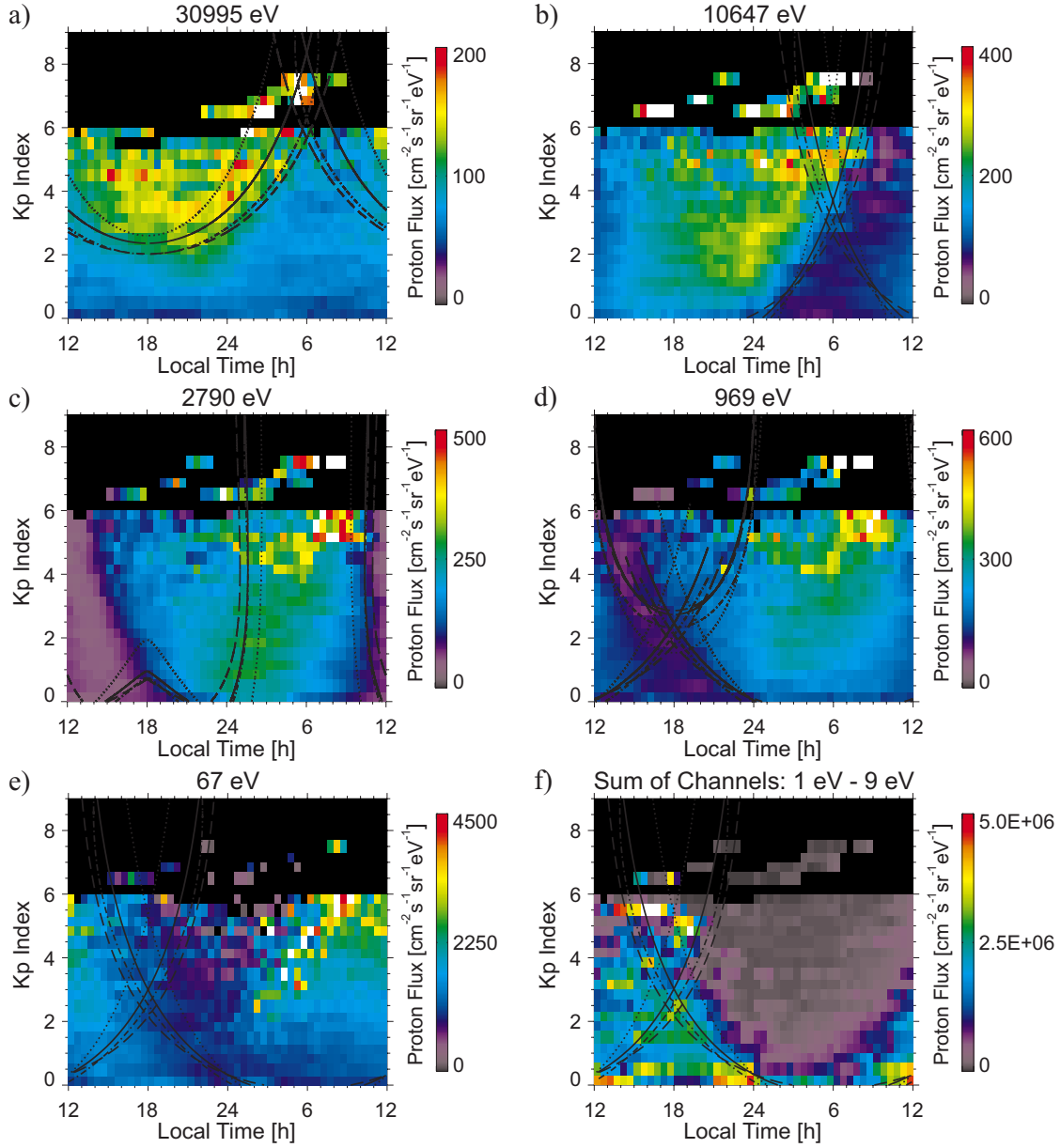


**Plate 2.** The 1996-averaged proton flux for six different energy channels, (a) 30,995 eV, (b) 10,647 eV, (c) 2790 eV, (d) 969 eV, (e) 67 eV, and (f) sum of 1–9 eV, binned according to LT and  $Kp$ . Black indicates no data available, and white bins contain fluxes that exceed the corresponding maximum of the color bar. The overlaid curves represent the local times of geosynchronous Alfvén layer crossings as a function of the  $Kp$  index (see also Figure 1) for the Gussenhoven model (dotted curve,  $\gamma = 1$ ; solid curve,  $\gamma = 2$ ; dashed curve,  $\gamma = 3$ ) and the Maynard model (dash-dotted curve,  $\gamma = 2$ ).



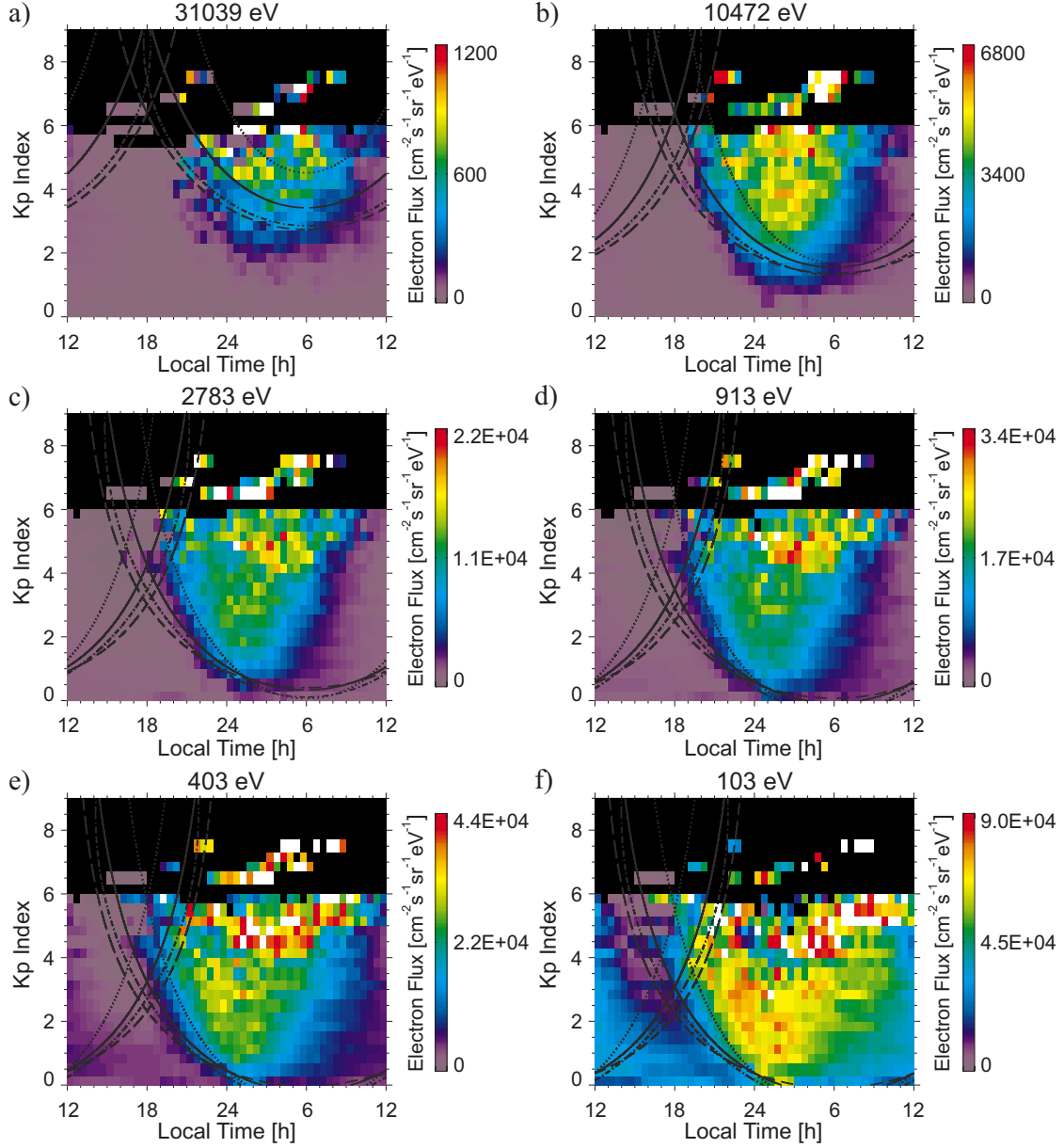


**Plate 3.** The 1996-averaged electron flux for six different energy channels, (a) 31,039 eV, (b) 10,472 eV, (c) 2783 eV, (d) 913 eV, (e) 403 eV, and (f) 103 eV, binned according to LT and  $Kp$ . Black indicates no data available, and white bins contain fluxes that exceed the corresponding maximum of the color bar. The overlaid curves represent the local times of geosynchronous Alfvén layer crossings as a function of the  $Kp$  index (see also Figure 2) for the Gussenhoven model (dotted curve,  $\gamma = 1$ ; solid curve,  $\gamma = 2$ ; dashed curve,  $\gamma = 3$ ) and the Maynard model (dash-dotted curve,  $\gamma = 2$ ).

bowsky, 1974; Elphic *et al.*, 1996, 1997; Borovsky *et al.*, 1998]. In addition, plasma sheet flux tubes that are originally empty of cold plasma are “refilled” (or, more properly, “filled”) with outflowing ionospheric material as they convect across the dayside magnetosphere [e.g., Chappell, 1972; Thomsen *et al.*, 1998; Lawrence *et al.*, 1999], which also leads to higher cold-proton fluxes in the afternoon sector. The shape of the evening flux boundary in Plate 2f is best approximated with the Gussenhoven  $\gamma = 1$  method.

The statistical distribution of the 67 eV ions (Plate 2e) does not appear to be organized by any of the calculated open-closed drift boundaries, which raises the question of what may be the source of this population. The plasma sheet is usually too hot to be a good source at these energies. On the other hand, unlike the cold plasma, these particles do not seem to build up in the closed drift region, suggesting that ionospheric refilling processes are not the source. Rather, the source appears to be on open drift trajectories after midnight, particularly at higher activity. This population may be produced by auroral upflows, or it might represent the low-energy edge of a cooler dawnside plasma sheet. An analysis of the pitch angle distribution of these ions may help discriminate between these possibilities.

#### 4.2. Electrons

The electron flux statistics (Plate 3) are also consistent with the hypothesis that the particle flux boundaries depend on a global convection pattern, coupled with loss processes (in this case, precipitation rather than charge exchange).

The electron drift pattern is much simpler than the drift pattern of the protons since the sum of gradient and corotation drift always results in a counterclockwise motion of the electrons around the Earth. Thus the bulge of the electron Alfvén layers is always at dusk, and there are no banana-shaped drift orbits as there were for the lower-energy protons. For higher energies (e.g. 31,039 eV, Figure 2a), geosynchronous orbit should be completely embedded in the trapped orbit region for  $Kp$  values below  $\sim 3$ , leading to low electron fluxes of these energies at all local times, as seen in the statistics (Plate 3a). As the geomagnetic activity increases, the Alfvén layer moves closer to the Earth, exposing geosynchronous orbit to the plasma sheet for an increasingly wide local time interval centered at 600 LT. For all electron energies the most distinct Alfvén layer crossing in Plate 3 is the transition from the trapped to open drift trajectories in the premidnight region. As the electrons move to the dayside, they precipitate rapidly into the ionosphere, causing the fluxes to decrease [e.g., Thomsen *et al.*, 1998]. By the time geosynchronous orbit enters the trapped orbit region on the dayside, the electron fluxes in the open drift trajectory region are so far depleted that the crossing is not detectable. This

observed behavior is the same for lower-energy channels as well. The appropriate shielding exponent implied by the observations in Plate 3 seems to be energy dependent: While the statistical boundaries of higher-energy channels are best fit by the Gussenhoven  $\gamma = 3$  model or the Maynard model, the Gussenhoven model with a smaller shielding exponent provides a better match at lower energies.

## 5. Discussion

### 5.1. Access

The observations show that the average plasma sheet access to geosynchronous orbit varies with local time,  $Kp$  index, and particle species and energy. Moreover, the shapes of the apparent observational boundaries of the differential fluxes in Plates 2 and 3 are consistent with the flux boundary curves calculated by a relatively simple electric field model. This leads to the conclusion that an electric field consisting of a superposition of a shielded cross-tail electric field and a corotation field is suitable for modeling average conditions at geosynchronous orbit. The boundaries between open and closed drift regions on the nightside are particularly clear. The agreement between observations and this model confirms that the  $Kp$  index provides an appropriate parametrization of the convection electric field.

On the dayside the model boundaries between open and closed drift trajectories are often invisible. Potentially, this could happen if the average convection changes on timescales shorter than the particle drift time. However, an analysis of the autocorrelation time of the  $Kp$  index, which is a measure of the persistence time of the geomagnetic activity, results in values of 33 hours or greater, depending on the year analyzed. This time is long compared to a typical drift time of  $\sim 12$  hours. Thus the flux measurements can be considered correctly binned, and the dayside view is just a time-lagged view of the nightside. More likely, the absence of discernible dayside boundaries is due to the fact that the fluxes have been greatly diminished by the time they reach this region. This strong depletion at essentially all energies supplies clear evidence for the operation of loss processes such as ion charge exchange and electron precipitation mentioned in section 4.

A definite determination of the shielding exponent for the convection electric field cannot be made from the results presented here because we have compared the statistics for spin-averaged fluxes with the predictions for  $90^\circ$  pitch angle particles. Preliminary calculations for  $K \neq 0$  particles suggest that, especially for the higher-energy channels, the model boundaries are very sensitive to the pitch angle. This may explain why the preferred shielding exponent appears to be energy dependent (Plates 2 and 3). Nevertheless, a shield-

ing exponent of  $\sim 2$  appears to provide a suitable match to the observed boundaries. More precise statements concerning the shielding exponent could potentially be made using the data set with pitch angle resolved, but this is beyond the scope of this paper.

The low-energy proton channels (Plates 2c–2e) and the low-energy electron channels (Plates 3e and 3f) show particularly high fluxes in the prenoon sector for higher geomagnetic activity levels. These high fluxes are not related to spacecraft charging since our analysis procedure specifically rejects fluxes that may be affected by charging.

## 5.2. Applications

Besides the differential fluxes, the MPA database also contains various plasma parameters that are obtained from the fluxes through moments calculations [Thomsen *et al.*, 1999]. As mentioned in section 1, these bulk properties are often used as boundary conditions in ring current simulations. The density and temperature are calculated separately for the lower-energy channels from 1 to 100 eV and for the higher-energy range from 100 eV to 40 keV. The density and temperature statistics for the higher-energy populations of each species at geosynchronous orbit are shown in Plates 4a–4d in the same format as the flux plots in Plates 2 and 3. Because these bulk moments represent weighted sums of the different energy channels, the statistical distributions shown in Plate 4 can be readily understood by reference to the distributions shown in Plates 2 and 3 for the individual energy levels.

**5.2.1. Density.** On the nightside the density profiles (Plates 4a and 4b) represent the average access of plasma sheet material to geosynchronous orbit. For  $Kp$  values  $\lesssim 3$ , electron and proton density profiles peak near local midnight and decrease toward dawn and dusk. The electron density (Plate 4b) shows a rapid density decrease from midnight to dusk caused by lack of electron access to geosynchronous orbit (see Plate 3). The resulting dark lane on the eveningside represents a region dominated by closed drift trajectories for electrons in the main plasma sheet energy range of a few hundred to a few thousand eV. The electron density decrease toward dawn can be explained by loss processes mainly due to electron precipitation.

For the protons the density distribution similarly reflects the flux distribution for the main plasma sheet ion energy range, approximately a few keV to a few tens of keV (compare Plates 2b and 2c). The decline in density from midnight toward dawn reflects the lack of dawnside access for plasma sheet ions of  $\sim 10$  keV, while the density decrease from midnight toward dusk is at least partly attributable to the exclusion of plasma sheet ions with energies  $\sim 1$  to a few keV. At higher values of  $Kp$  there is a persistent dawn-dusk asym-

metry in the proton density that would not seem to be due to lack of access to plasma sheet trajectories. Rather, the asymmetry may be due to the fact that the ions take longer to drift to the duskside than the dawnside, with correspondingly greater losses. The further reductions in ion density toward noon are clearly evidence for such losses [Maurice *et al.*, 1998].

A further interesting aspect of the ion and electron density distributions in Plates 4a and 4b is the clear tendency to see higher densities at  $Kp \gtrsim 4$ , especially on the dawnside. These increases occur essentially across the entire primary plasma sheet energy range for both species (see Plates 2 and 3). We do not presently have an explanation for these enhanced densities. However, a study on the central plasma sheet by Wing and Newell [1998] reveals high proton densities along the dawnside low-latitude boundary layer. This high-density region moves closer to the Earth as the geomagnetic activity level increases. Drifting on the right trajectories, these particles could cause the geosynchronous density to be enhanced at dawn during these times, but the use of more sophisticated models for the magnetic and electric field will be necessary to pursue this question.

**5.2.2. Temperature.** While the density profiles show the average access of plasma sheet particles to geosynchronous orbit, the temperature profiles reflect primarily the accessibility of high-energy particles. The ion temperature profile shows a cool region at dawn, which is a region of trapped orbits for the higher-energy plasma sheet particles. Increasing  $Kp$  allows high-energy particles access to geosynchronous orbit over a broader local time range.

Similarly, in the electron temperature profile, the band of low temperatures in the dusk region identifies the LT range where only the lower-energy portion of the plasma sheet has access. The high-energy electrons can reach geosynchronous orbit only at  $Kp$  values  $\geq 2$ –, explaining the low electron temperatures over the entire orbit for small  $Kp$  values. At high  $Kp$  the high electron temperatures in the postmidnight region are due to the substorm injection and subsequent drift of energetic plasma sheet electrons.

The preceding discussion suggests that caution should be used in making comparisons of the geosynchronous density and temperature statistics with magnetotail values of these parameters: Since higher-energy plasma sheet particles cannot access geosynchronous orbit at low  $Kp$  values, the full plasma sheet population is not sampled there at such times. Furthermore, as noted above, the temperatures shown in Plate 4 have been calculated based on observed fluxes up to only  $\sim 40$  keV. They may thus underestimate the true temperature during times when particles at higher energies are present in abundance [e.g., Birm *et al.*, 1997]. This is primarily a problem for the ion population.

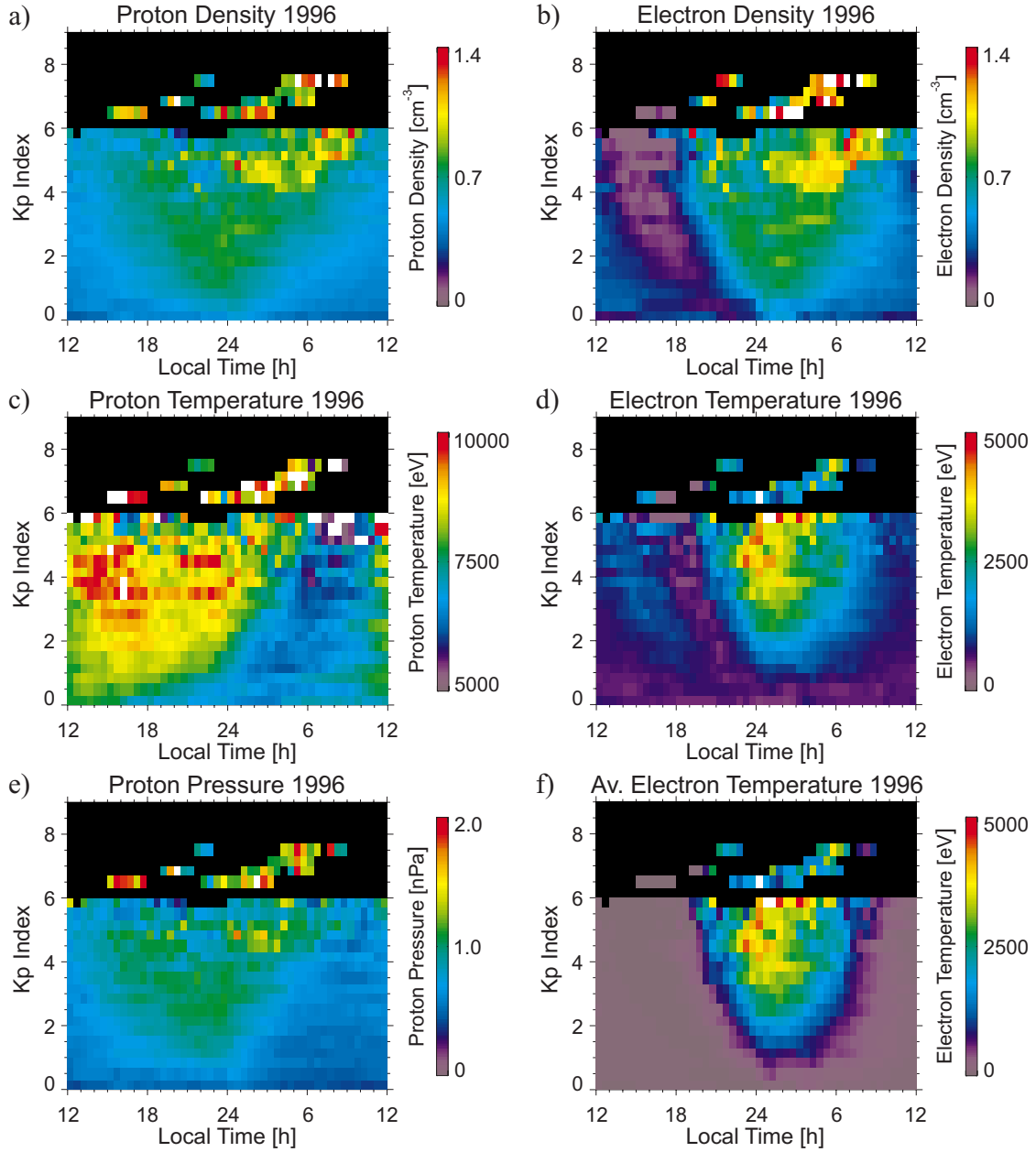


**Plate 4.** Geosynchronous bulk properties: (a) proton density, (b) electron density, (c) perpendicular proton temperature, (d) perpendicular electron temperature, (e) proton pressure, (f) average electron temperature.

**5.2.3. Proton pressure.** Multiplication of the proton density and temperature measurements result in the proton pressure (Plate 4e). The pressure distribution is an indication of where currents are flowing, since the current density is related to the pressure gradient by  $j_{\perp} \approx (\mathbf{B} \times \nabla p)/B^2$ . Even though the proton density and temperature have significant azimuthal gradients on the nightside, the two quantities seem to balance each other, producing a more nearly uniform proton pressure across the nightside magnetosphere. This suggests that at geosynchronous orbit, radial currents in the equatorial plasma sheet are rather small.

**5.2.4. Spacecraft charging.** In a thick sheath approximation, where the Debye length is large compared to the spacecraft radius (which generally applies to geosynchronous satellites since for a typical plasma sheet density of  $n = 1 \text{ cm}^{-3}$  and an electron temperature of  $T_e \gtrsim 200 \text{ eV}$ , the Debye length is  $\lambda_D \gtrsim 100 \text{ m}$ ), the spacecraft surface potential relative to the ambient plasma is given by  $V \approx -\langle T_E \rangle$  [Garrett and Rubin, 1978; Garrett, 1981]. The average electron temperature  $\langle T_E \rangle$  can be calculated by combining the properties of low- and high-energy electrons:

$$\langle T_E \rangle = \frac{n_{le} T_{le} + n_{he} T_{he}}{n_{le} + n_{he}}, \quad (10)$$

where  $n_{le/he}$  and  $T_{le/he}$  are electron density and temperature for low energies (le) and high energies (he), respectively. As discussed by other authors [e.g., McComas *et al.*, 1993], the MPA instruments typically float somewhat negative relative to the ambient plasma. Hence low-energy ambient electrons are repelled from the spacecraft. Furthermore, because of differential surface charging effects, the low-energy electron measurements are also contaminated by trapped photoelectrons. Therefore, to estimate  $\langle T_E \rangle$ , the low-energy electron density  $n_{le}$  in (10) is replaced by the measured density of low-energy protons  $n_{lp}$ , under the assumption that the two densities are approximately equal. In addition, the temperature of the low-energy electrons  $T_{le}$  is estimated to be 5 eV. (The value chosen for  $T_{le}$  is of little importance for the outcome of the statistics.) The statistics of the resulting average electron temperature at geosynchronous orbit (Plate 4f) show high values on the nightside magnetosphere, especially between midnight and dawn, indicating the likelihood of significant surface charging for spacecraft moving through this region. A similar observation has been made by McPherson *et al.* [1975], who analyzed operational anomalies of several satellites, which occurred mainly between 2300 LT and 600 LT. Those authors identified charge buildup through intense fluxes of energetic electrons associated with substorm injection events as the cause of the satellite operating anomalies. The statistics in Plate 4f also indicate a  $Kp$  dependence on the average electron temperature, as observed by Garrett

and Rubin [1978]: the higher the geomagnetic activity level, the higher the average electron temperature found.

### 5.3. Comparison With ATS Measurements

A previous analysis of the statistical properties of the geosynchronous plasma environment was reported by Garrett *et al.* [1981a, b] from ATS 5 and ATS 6 measurements. Among other things these authors examined the local time dependence of density and temperature at geosynchronous orbit. Their results are compared with the MPA statistics in Figure 4 for three  $Kp$  values approximately matching the most common values during the ATS measurements.

The local time dependence of the MPA and ATS 5 proton densities shows the same qualitative behavior, even though the absolute values differ about a factor of  $\sim 2$  (Figure 4a). This discrepancy may be due to differences in the energy ranges of the instruments and the method chosen for the moments calculation. The ATS 6 proton density curve differs vastly from the other measurements because it includes measurements that extend down to  $\sim 1 \text{ eV}$ , whereas ATS 5 extends down to 50 eV [Garrett *et al.*, 1981b] and the MPA (high energy component) density includes only measurements above 100 eV. The MPA proton density shows only a very slight dependence on the geomagnetic activity level in the  $Kp$  range between 1 and 3, which is in agreement with analysis of the ATS data [cf. Garrett *et al.*, 1981b, Figure 3a].

The qualitative dependence of the MPA electron density on local time is in agreement with both the ATS 5 and ATS 6 measurements, although the absolute value is instrument dependent (Figure 4b). Furthermore, the independence of the MPA electron density on the  $Kp$  index in the range shown in the graph agrees with the results of the ATS study [cf. Garrett *et al.*, 1981a, Figure 4].

The ATS and MPA statistics also agree qualitatively with respect to the proton temperature (Figure 4c). The absolute values of the ATS 6 data seem to be closer to the MPA data, while the shape of the MPA proton temperature curve is closer to the ATS 5 data. The  $Kp$  dependence of the MPA data is negligible, just as shown by Garrett *et al.* [1981b].

The MPA curves for the electron temperature (Figure 4d) agree with the ATS 6 statistics, while the ATS 5 data contradict these results. The reason for this deviation suggested by Garrett *et al.* [1981a] is the more quiescent magnetosphere sampled by the ATS 5 satellite. However, our results do not show a dusk enhancement in  $T_e$  during quiet times, as indicated by the ATS 5 measurements. Rather, the primary  $Kp$  effect on the geosynchronous electron temperature distribution appears from our results to be an increase in the

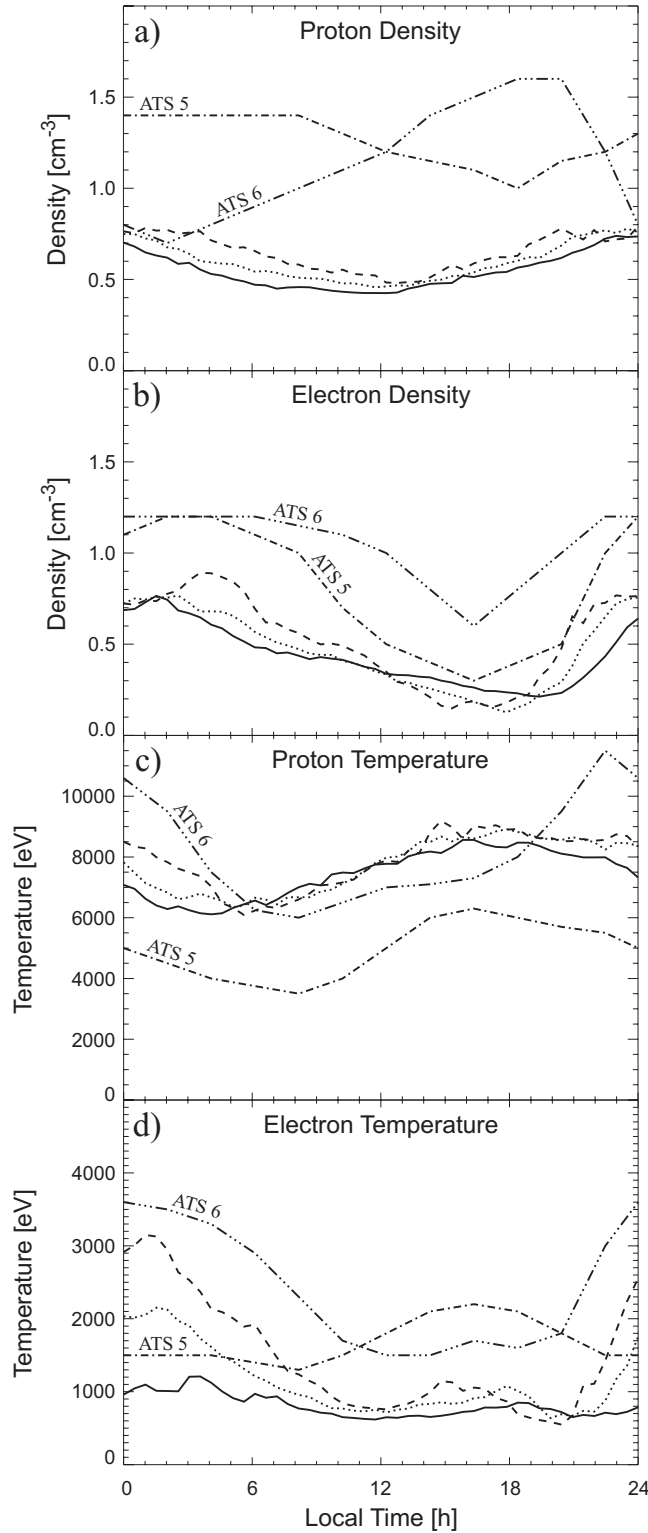


**Figure 4.** Comparison of (a) proton and (b) electron density and (c) proton and (d) electron temperature moments calculated from MPA with ATS 5 and 6 measurements. The MPA moments are shown for  $Kp$  values 1 (solid curve), 2 (dotted curve), and 3 (dashed curve). The ATS 5 and 6 measurements are plotted by dash-dotted curves and dash-dot-dot-dotted curves, respectively.

average nightside temperature with increasing activity.

## 6. Summary

Using 1 year's worth of magnetospheric plasma analyzer data from three Los Alamos geosynchronous satellites, a statistical study has been made of the LT and  $Kp$  dependence of proton and electron fluxes at geosynchronous orbit. Displayed as a function of the two independent parameters LT and  $Kp$ , the fluxes show distinct boundaries that result from a global magnetospheric particle drift process combined with losses due to charge exchange of the ions and auroral precipitation of the electrons. The observational boundaries have been compared with theoretical positions of separatrices between open and closed drift trajectories calculated by a Hamiltonian energy conservation approach. Using a coordinate transformation from Cartesian space to the  $(U, B, K)$  space, the position of the Alfvén layers as a function of particle species, energy, local time, and geomagnetic activity level can be obtained easily. The result confirms the predictions of plasma sheet access to the geosynchronous region. The statistical distributions presented here have numerous potential practical applications, such as providing appropriate initial or boundary conditions for simulations of ring current evolution.

Selected plasma bulk properties such as the density, temperature, proton pressure, and the average electron temperature, which are obtained from the fluxes, were also statistically evaluated. The shape of the resulting moments distributions can be explained by the access pattern combined with loss processes as discussed for the fluxes. The distribution of the average electron temperature, which is a proxy for spacecraft charging, shows high values in the postmidnight region. The average electron temperature also tends to increase with higher geomagnetic activity.

Furthermore, the statistics of the bulk properties have been compared to a previous statistical analysis of the geosynchronous plasma environment by *Garrett et al.* [1981a, b] from ATS 5 and ATS 6 measurements. Even though the absolute values of the plasma properties determined from the two data sets differ from each other because of the different energy ranges used in the ATS calculations, the qualitative dependences of MPA and ATS 5 and 6 measured plasma properties on local time are in agreement with each other.

**Acknowledgments.** The authors would like to express our appreciation to E. C. Whipple, R. B. Sheldon, and S. Maurice for considerable help in understanding the  $(U, B, K)$  coordinate system. We also thank K.-H. Glaßmeier and the MPA team at LANL for helpful discussions and comments. We especially thank D. M. Delapp and E. J. Noveroske for assisting us with the large amount of data processed for this paper. Finally, we thank both

referees for their helpful suggestions. This work was carried out under the auspices of the U. S. Department of Energy, with partial support from the NASA ISTP program.

Janet G. Luhmann thanks Michael Liemohn and another referee for their assistance in evaluating this paper.

## References

- Bame, S. J., D. J. McComas, M. F. Thomsen, B. L. Barraclough, R. C. Elphic, and J. P. Glore, Magnetospheric plasma analyzer for spacecraft with constrained resources, *Rev. Sci. Instrum.*, **64**, 1026–1033, 1993.
- Birn, J., M. F. Thomsen, J. E. Borovsky, G. D. Reeves, D. J. McComas, and R. D. Belian, Characteristic plasma properties during dispersionless substorm injections at geosynchronous orbit, *J. Geophys. Res.*, **102**, 2309–2324, 1997.
- Borovsky, J. E., M. F. Thomsen, D. J. McComas, T. E. Cayton, and D. J. Knipp, Magnetospheric dynamics and mass flow during the November 1993 storm, *J. Geophys. Res.*, **103**, 26,373–26,394, 1998.
- Burke, W. J., A. G. Rubin, and D. A. Hardy, Banded electron structures in the plasmasphere, *J. Geophys. Res.*, **100**, 7759–7769, 1995.
- Chappell, C. R., Recent satellite measurements of the morphology and dynamics of the plasmasphere, *Rev. Geophys.*, **10**, 951–979, 1972.
- Chen, A. J., and J. M. Grebowsky, Plasma tail interpretations of pronounced detached plasma regions measured by Ogo 5, *J. Geophys. Res.*, **79**, 3851–3855, 1974.
- Chen, M. W., L. R. Lyons, and M. Schulz, Simulations of phase space distributions of storm time proton ring current, *J. Geophys. Res.*, **99**, 5745–5759, 1994.
- DeForest, S. E., and C. E. McIlwain, Plasma clouds in the magnetosphere, *J. Geophys. Res.*, **76**, 3587–3611, 1971.
- Ejiri, M., Trajectory traces of charged particles in the magnetosphere, *J. Geophys. Res.*, **83**, 4798–4810, 1978.
- Ejiri, M., R. A. Hoffman, and P. H. Smith, The convection electric field model for the magnetosphere based on EXPLORER 45 observations, *J. Geophys. Res.*, **83**, 4811–4815, 1978.
- Elphic, R. C., L. A. Weiss, M. F. Thomsen, and D. J. McComas, Evolution of plasmaspheric ions at geosynchronous orbit during times of high geomagnetic activity, *Geophys. Res. Lett.*, **23**, 2189–2192, 1996.
- Elphic, R. C., M. F. Thomsen, and J. E. Borovsky, The fate of the outer plasmasphere, *Geophys. Res. Lett.*, **24**, 365–368, 1997.
- Elphic, R. C., M. F. Thomsen, J. E. Borovsky, and D. J. McComas, The inner edge of the electron plasma sheet: Empirical models of boundary location, *J. Geophys. Res.*, in press, 1999.
- Fok, M.-C., J. U. Kozyra, and A. F. Nagy, Lifetime of ring current particles due to Coulomb collisions in the plasmasphere, *J. Geophys. Res.*, **96**, 7861–7867, 1991.
- Fok, M.-C., T. E. Moore, and M. E. Greenspan, Ring current development during storm main phase, *J. Geophys. Res.*, **101**, 15,311–15,322, 1996.
- Garrett, H. B., The charging of spacecraft surfaces, *Rev. Geophys.*, **19**, 577–616, 1981.
- Garrett, H. B., and A. G. Rubin, Spacecraft charging at geosynchronous orbit – Generalized solution for eclipse passage, *Geophys. Res. Lett.*, **5**, 865–868, 1978.
- Garrett, H. B., D. C. Schwank, and S. E. Deforest, A statistical analysis of the low-energy geosynchronous plasma environment, I, Electrons, *Planet. Space Sci.*, **29**, 1021–1044, 1981a.
- Garrett, H. B., D. C. Schwank, and S. E. Deforest, A statistical analysis of the low-energy geosynchronous plasma environment, II, Ions, *Planet. Space Sci.*, **29**, 1045–1060, 1981b.
- Gussenhoven, M. S., D. A. Hardy, and W. J. Burke, DMSP/F2 electron observations of equatorward auroral boundaries and their relationship to magnetospheric electric fields, *J. Geophys. Res.*, **86**, 768–778, 1981.
- Gussenhoven, M. S., D. A. Hardy, and N. Heinemann, Systematics of the equatorward diffuse auroral boundary, *J. Geophys. Res.*, **88**, 5692–5708, 1983.
- Jordanova, V. K., L. M. Kistler, J. U. Kozyra, G. V. Khazanov, and A. F. Nagy, Collisional losses of ring current ions, *J. Geophys. Res.*, **101**, 111–126, 1996.
- Jordanova, V. K., et al., October 1995 magnetic cloud and accompanying storm activity: Ring current evolution, *J. Geophys. Res.*, **103**, 79–92, 1998.
- Kerns, K. J., D. A. Hardy, and M. S. Gussenhoven, Modeling of convection boundaries seen by CRRES in 120-eV to 28-keV particles, *J. Geophys. Res.*, **99**, 2403–2414, 1994.
- Kistler, L. M., F. M. Ipavich, D. C. Hamilton, G. Gloeckler, B. Wilken, G. Kremser, and W. Stüdemann, Energy spectra of the major ion species in the ring current during geomagnetic storms, *J. Geophys. Res.*, **94**, 3579–3599, 1989.
- Kivelson, M. G., and C. T. Russell, *Introduction to Space Physics*, Cambridge Univ. Press, New York, 1995.
- Kozyra, J. U., M.-C. Fok, E. R. Sanchez, D. S. Evans, D. C. Hamilton, and A. F. Nagy, The role of precipitation losses in producing the rapid early recovery phase of the Great Magnetic Storm of February 1986, *J. Geophys. Res.*, **103**, 6801–6814, 1998a.
- Kozyra, J. U., V. K. Jordanova, J. E. Borovsky, M. F. Thomsen, D. J. Knipp, D. S. Evans, D. J. McComas, and T. E. Cayton, Effects of a high-density plasma sheet on ring current development during the November 2–6, 1993, magnetic storm, *J. Geophys. Res.*, **103**, 26,285–26,305, 1998b.
- Lawrence, D. J., M. F. Thomsen, J. E. Borovsky, and D. J. McComas, Measurements of early and late-time plasmasphere refilling as observed from geosynchronous orbit, *J. Geophys. Res.*, **104**, 14,691–14,704, 1999.
- Liemohn, M. W., G. V. Khazanov, and J. U. Kozyra, Banded electron structure formation in the inner magnetosphere, *Geophys. Res. Lett.*, **25**, 877–880, 1998.
- Maurice, S., M. F. Thomsen, D. J. McComas, and R. C. Elphic, Quiet time densities of hot ions at geosynchronous orbit, *J. Geophys. Res.*, **103**, 17,571–17,585, 1998.
- Maynard, N. C., and A. J. Chen, Isolated cold plasma regions: Observations and their relation to possible production mechanisms, *J. Geophys. Res.*, **80**, 1009–1013, 1975.
- McComas, D. J., S. J. Bame, B. L. Barraclough, J. R. Donart, R. C. Elphic, J. T. Gosling, M. B. Moldwin, K. R. Moore, and M. F. Thomsen, Magnetospheric plasma analyzer: Initial 3-spacecraft observations from geosynchronous orbit, *J. Geophys. Res.*, **98**, 13,453–13,465, 1993.

- McIlwain, C. E., Plasma convection in the vicinity of the geosynchronous orbit, in *Earth's Magnetospheric Processes*, edited by B. M. McCormac, pp. 268–279, D. Reidel, Norwell, Mass., 1972.
- McPherson, D. A., D. P. Cauffman, and W. R. Schober, Spacecraft charging at high-altitudes: SCATHA satellite program, *J. Spacecr. Rockets*, 12, 621–626, 1975.
- Nishida, A., Formation of plasmopause, or magnetospheric plasma knee, by the combined action of magnetospheric convection and plasma escape from the tail, *J. Geophys. Res.*, 71, 5669–5679, 1966.
- Roederer, J. G., *Dynamics of Geomagnetically Trapped Radiation*, vol. 2 of *Physics and Chemistry in Space*, Springer, New York, 1970.
- Schild, M. A., J. W. Freeman, and A. J. Dessler, A source for field-aligned currents at auroral latitudes, *J. Geophys. Res.*, 74, 247–256, 1969.
- Smith, P. H., N. K. Bewtra, and R. A. Hoffman, Motions of charged particles in the magnetosphere under the influence of a time-varying large scale convection electric field, in *Quantitative Modeling of Magnetospheric Processes*, *Geophys. Monogr. Ser.* vol. 21, edited by W. P. Olsen, pp. 513–534, AGU, Washington, D.C., 1979.
- Southwood, D. J., and S. M. Kaye, Drift boundary approximations in simple magnetospheric convection models, *J. Geophys. Res.*, 84, 5773–5780, 1979.
- Stern, D. P., Motion of a proton in the equatorial magnetosphere, *J. Geophys. Res.*, 80, 595–599, 1975.
- Taylor, H. E., and E. W. Hones, Adiabatic motion of auroral particles in a model of the electric and magnetic fields surrounding the earth, *J. Geophys. Res.*, 70, 3605–3628, 1965.
- Thomsen, M. F., D. J. McComas, J. E. Borovsky, and R. C. Elphic, The magnetospheric trough, in *Geospace Mass and Energy Flow: Results From the International Solar-Terrestrial Physics Program*, *Geophys. Monogr. Ser.* vol. 104, edited by J. L. Horwitz et al., pp. 355–369, AGU, Washington, D.C., 1998.
- Thomsen, M. F., E. Noveroske, J. E. Borovsky, and D. J. McComas, Calculation of moments from measurements by the Los Alamos magnetospheric plasma analyzer, *LA Rep. LA-13566-MS*, Los Alamos Nat. Lab., Los Alamos, N. M., 1999.
- Volland, H., A semiempirical model of large-scale magnetospheric electric fields, *J. Geophys. Res.*, 78, 171–180, 1973.
- Whipple, E. C., (U,B,K) coordinates: A natural system for studying magnetospheric convection, *J. Geophys. Res.*, 83, 4318–4326, 1978.
- Wing, S., and P. T. Newell, Central plasma sheet ion properties as inferred from ionospheric observations, *J. Geophys. Res.*, 103, 6785–6800, 1998.
- Wolf, R. A., M. Harel, R. W. Spiro, G. H. Voigt, P. H. Reiff, and C. K. Chen, Computer simulation of inner magnetospheric dynamics for the magnetic storm of July 29, 1977, *J. Geophys. Res.*, 87, 5949–5962, 1982.
- J. E. Borovsky, H. Korth, D. J. McComas, and M. F. Thomsen, Space and Atmospheric Science, Los Alamos National Laboratory, NIS-1, MS D466, Los Alamos, NM 87545. (hkorth@lanl.gov)
- May 17, 1999; revised June 28, 1999; accepted June 28, 1999.

---

This preprint was prepared with AGU's L<sup>A</sup>T<sub>E</sub>X macros v4, with the extension package 'AGU++' by P. W. Daly, version 1.5g from 1998/09/14.